ACS APPLIED MATERIALS & INTERFACES

Research Article

www.acsami.org

Releasing Metal Catalysts via Phase Transition: $(NiO)_{0.05}$-$(SrTi_{0.8}Nb_{0.2}O_3)_{0.95}$ as a Redox Stable Anode Material for Solid Oxide Fuel Cells

Guoliang Xiao,[†] Siwei Wang,[†] Ye Lin,[†] Yanxiang Zhang,[†,‡] Ke An,[§] and Fanglin Chen*[,†]

[†]Department of Mechanical Engineering, University of South Carolina, Columbia, South Carolina 29208, United States

[‡]School of Materials Science and Engineering, Harbin Institute of Technology, Harbin, Heilongjiang 150001, China

[§]Chemical and Engineering Materials Division, Oak Ridge National Laboratory, Oak Ridge, Tennessee 37831, United States

ABSTRACT: Donor-doped perovskite-type $SrTiO_3$ experiences stoichiometric changes at high temperatures in different P_{o2} involving the formation of Sr or Ti-rich impurities. NiO is incorporated into the stoichiometric strontium titanate, $SrTi_{0.8}Nb_{0.2}O_{3-\delta}$ (STN), to form an A-site deficient perovskite material, $(NiO)_{0.05}$-$(SrTi_{0.8}Nb_{0.2}O_3)_{0.95}$ (Ni-STN), for balancing the phase transition. Metallic Ni nanoparticles can be released upon reduction instead of forming undesired secondary phases. This material design introduces a simple catalytic modification method with good compositional control of the ceramic backbones, by which transport property and durability of solid oxide fuel cell anodes are largely determined. Using Ni-STN as anodes for solid oxide fuel cells, enhanced catalytic activity and remarkable stability in redox cycling have been achieved. Electrolyte-supported cells with the cell configuration of Ni-STN-SDC anode, $La_{0.8}Sr_{0.2}Ga_{0.87}Mg_{0.13}O_3$ (LSGM) electrolyte, and $La_{0.6}Sr_{0.4}Co_{0.2}Fe_{0.8}O_3$ (LSCF) cathode produce peak power densities of 612, 794, and 922 mW cm^{-2} at 800, 850, and 900 °C, respectively, using H_2 as the fuel and air as the oxidant. Minor degradation in fuel cell performance resulted from redox cycling can be recovered upon operating the fuel cells in H_2. Such property makes Ni-STN a promising regenerative anode candidate for solid oxide fuel cells.

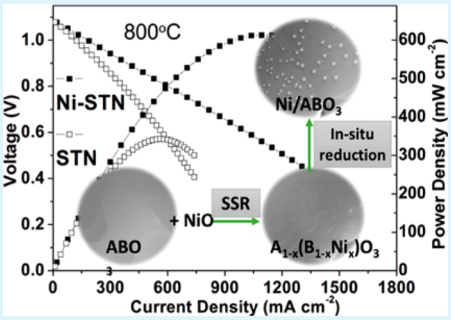

KEYWORDS: *SOFC, catalysis, ceramics, electrode, nanoparticles, redox*

1. INTRODUCTION

Solid oxide fuel cells (SOFCs) possess high conversion efficiency and fuel flexibility and have been considered as one of the most versatile clean energy technologies.[1,2] Conventional Ni-cermet anode materials for SOFCs have unique merits such as low cost, ease of processing, and excellent electrochemical activity for typical fuels, but they suffer from several instability issues.[3−5] Among them, the redox cycling instability, arisen from the substantial volume change of Ni, causes severe performance degradation and even failure of SOFCs, and redox cycling may be unavoidable during the long-term operation of SOFCs.[6] Considerable efforts have been devoted to solve such issues by developing alternative redox stable anode materials.[7]

Although ceramic materials have been proposed to address the redox instability issues of SOFC anodes, their generally low catalytic activity for fuel oxidation significantly limits fuel cell performance compared to Ni-cermet anodes.[8−11] Additional catalyst loading through infiltration has been generally applied to enhance the anode catalytic activity.[12−16] Compared with conventional deposition methods, ceramic materials that can self-extract catalysts during operation become very attractive for their simplicity to be scaled up.[17−21] Recently, some other materials have also been designed to form catalyst particles by introducing large amounts of cation vacancy and reducing the ceramic phase stability.[22,23] Some of these materials are summarized in Table 1. However, the major limitation for these materials is the less-controlled ceramic composition change. Extracting catalysts from the ceramic phase causes compositional change, by which the transport property and durability of the anode are largely determined.[24] In some cases, the ceramic phase gradually decomposes while generating metallic catalysts. It causes the catalyst particles to be blocked from connecting to the conductive network and become electrochemically inactive. The cell performance may not be improved and may even degrade.[21,23,25] Therefore, besides obtaining nanocatalysts, carefully tailoring the composition of the reduced ceramics is essential for achieving active and stable performance in applications. However, so far little attention has been paid to the reduced ceramic phases in these material systems. Here we demonstrate a strategy to store Ni catalysts via phase transition of Nb doped $SrTiO_3$. Nanosized metallic catalysts are extracted under anode conditions, while the ceramic composition gradually approaches the anticipated stoichiometry without forming undesirable secondary phases. Enhanced catalytic activity and remarkable stability in redox cycling have been achieved.

Received: August 17, 2014
Accepted: October 21, 2014
Published: October 21, 2014

Table 1. Ceramic Materials Self-Extracting Catalysts upon in Situ Reduction

initial composition	catalysts (size), reduction temperature	ceramic phaseoh	ref
$La_{0.8}Sr_{0.2}Cr_{1-y}X_yO_{3-\delta}$, X = Ni, Ru, Pd, y =0−0.31, perovskite	Ru (<10 nm) Ni (10−50 nm) Pd (∼8 nm), 800 °C	perovksite phase + oxides	18, 19, 21
$NbTi_{0.5}Ni_{0.5}O_4$, rutile	Ni (<1 μm), 1000 °C	rutile $Nb_{1.33}Ti_{0.67}O_4$	20
$La_{0.52}Sr_{0.28}Ni_{0.06}Ti_{0.94}O_3$, $La_{0.8}Ce_{0.1}Ni_{0.4}Ti_{0.6}O_3$, perovskite	Ni (<50 nm), 930 °C	perovksite phase, perovksite phase + CeO_2	22
$Sr_{1.9}Fe_{1.4}Ni_{0.1}Mo_{0.5}O_{6-\delta}$, perovskite	Ni−Fe (10−50 nm), 800 °C	perovksite phase + oxides	23
$Pr_{0.4}Sr_{0.6}Co_{0.2}Fe_{0.7}Nb_{0.1}O_{3-\delta}$, perovskite	Fe−Co (∼50 nm), 900 °C	K_2NiF_4 -type $Pr_{0.8}Sr_{1.2}(Co,Fe)_{0.8}Nb_{0.2}O_{4+\delta}$	34

2. EXPERIMENTAL STUDY

2.1. Material Preparation. $(NiO)_{0.05}$-$(SrTi_{0.8}Nb_{0.2}O_{3-\delta})_{0.95}$ (Ni-STN) and $SrTi_{0.8}Nb_{0.2}O_{3-\delta}$ (STN) were synthesized by solid-state reactions starting from NiO (99%), $SrCO_3$ (99%), TiO_2 (99.9%), and Nb_2O_5 (99.9%) according to the stoichiometry. The mixed powder was first fired at 900 °C for 4 h in air and then ground and pressed into pellets. The solid state reaction was taken place at 1200 °C in air for 10 h and repeated another time to improve phase purity.

The obtained powder was mixed with 20 wt % graphite, pelletized, and sintered at 1400 °C in air for 10 h for making porous pellets. The porous pellets were reduced in H_2 (3 vol % H_2O) at 900 °C for 10 or 20 h for microstructure study. Ni-STN pellet was also reduced in 5% H_2 (balanced with N_2) at 1400 °C in a tubular furnace (MTI GSL1700S) for 10 h and then crushed into powder for TEM, neutron diffraction and XPS study.

For electrochemical characterization, $Ce_{0.8}Sm_{0.2}O_2$ (SDC), $La_{0.4}Ce_{0.6}O_2$ (LDC), and $La_{0.6}Sr_{0.4}Co_{0.2}Fe_{0.8}O_3$ (LSCF) were prepared by a citric-acid-assisted combustion method, and $La_{0.8}Sr_{0.2}Ga_{0.87}Mg_{0.13}O_3$ (LSGM) was synthesized by a solid-state reaction method.

2.2. Characterization and Electrochemical Evaluation. X-ray diffraction (XRD) data for the synthesized powders were collected on a D/MAX-3C X-ray diffractometer equipped with a graphite monochromator and Cu Kα radiation in a 2θ range of 20−80° at 5° min^{-1}. SEM images of fracture surface of the porous Ni-STN pellets were obtained by using a Zeiss Ultraplus Thermal Field Emission Scanning Electron Microscope. Only the sample before reduction was coated with Au due to the low conductivity. A JEOL2100F transmission electron microscope (TEM) equipped with a Schottky field-emission gun (FEG), with Cs = 1.0 mm operated at 200 kV was used to obtain high resolution TEM images on Ni-STN powder reduced at 1400 °C. Powder neutron diffraction data were collected using the VULCAN neutron powder diffractometer at the Spallation Neutron Source at Oak Ridge National Laboratory, and a vanadium sample canister was used for holding samples during test.[26,27] Rietveld refinement of the data was performed using the GSAS software package and the EXPGUI interface.[28] X-ray photoelectron spectroscopy (XPS) was conducted on a Kratos Axis Ultra DLD instrument.

LSGM pellets were sintered at 1450 °C for 10 h to form dense electrolyte membranes about 200 μm thick. An LDC interlayer was fabricated by painting LDC slurry on the anode side of the LSGM electrolyte membrane to prevent possible reactions between the anode materials and LSGM. The electrolyte membranes with the LDC interlayers were sintered at 1350 °C for 2 h. Ni-STN or STN with SDC (70:30 wt %) and pure LSCF were used as the anode and cathode materials. The electrode slurries as well as the LDC slurry were made by mixing the powders with a Heraeus binder V006 at a weight ratio of 1:1.5. The anode and cathode were then painted on the LSGM membrane and cofired in air at 1100 °C for 2 h. Au paste (Heraeus C5755A) and Pt paste (Heraeus CL11−5100) were painted on the anode and cathode, respectively, and fired at 1000 °C for 0.5 h to form the current collectors. The effective area of the cells was controlled by the cathode size, which is 0.33 cm^{-2}. Two wires were connected to each electrode and the cells were tested in a four-probe configuration. The flow rate of the fuel gas was set to 40 mL min^{-1}, and ambient air was used as the oxidant. A Versa STAT 3−400 test system (Princeton Applied Research) was used for electrochemical characterizations.

For the redox stability test, the anode was purged with N_2 for 10 min before switching the gas between air and H_2. After each cycle, the electrochemical impedance measurements were carried on in H_2 after the OCV became stable. After operating the cells under a constant current load in H_2, the impedance spectra were also measured before conducting another cycle.

The electrochemical processes detected by impedance spectroscopy were characterized by the distribution of relaxation time (DRT), $\gamma(\tau)$, where τ is the relaxation time. The core physics of DRT is that the impedance is a summation of infinite number of infinitely small RC elements. Mathematically, DRT is an implicit function of the imaginary part of polarization resistance, $Z''(\omega)$, given by,

$$Z''(\omega) = R_p \int_0^\infty \frac{\omega\tau}{1+(\omega\tau)^2}\gamma(\tau)d\tau \quad \text{with} \int_0^\infty \gamma(\tau)d\tau = 1 \tag{1}$$

where R_p is the DC activation resistance.

3. RESULTS AND DISCUSSION

Despite the low catalytic activity, donor dopants, such as La, Y, and Nb, doped $SrTiO_3$ materials are quite attractive among the explored ceramic SOFC anodes for their excellent stability and remarkably high electrical conductivity at low Po_2.[9,29−32] The stoichiometric change of these donor-doped $SrTiO_3$ materials has been reported. Taking Nb-doped $SrTiO_3$ as an example, phase transition from the strontium-deficient phase to the stoichiometric phase can be expected upon reduction ($P_{o2} \sim 10^{-20}$ atm, above 800 °C) involving Sr-rich or Ti/Nb-rich secondary phases, as shown by eqs 2 and 3.[33]

$$Sr_{1-x/2}Ti_{1-x}Nb_xO_3 + \frac{x}{2}SrO \xrightarrow{\text{anode}} SrTi_{1-x}Nb_xO_3 + \frac{x}{4}O_2,\ (0 \le x \le 1) \tag{2}$$

$$Sr_{1-x/2}Ti_{1-x}Nb_xO_3 \xrightarrow{\text{anode}} \left(1-\frac{x}{2}\right) SrTi_{(1-x-y)/(1-x/2)}Nb_{(x/2+y)/(1-x/2)}O_{(3-5x/2+3y)/(1-x/2)} + yTiO_2 + \left(\frac{x}{2}-y\right)Nb_2O_5,\ (0 \le y \le x/2 \le 0.5) \tag{3}$$

According to eq 2, the excess B-site cations in A-site deficient compositions can be replaced by transition metal oxides, which may be reduced to metallic catalyst under anodic conditions, and Ni is selected for its excellent catalytic activity among the nonprecious metals.[19,20,34] Incorporation of NiO into the stoichiometric perovskite STN can be expressed by eq 4.

$$y\mathrm{NiO} + (1-y)\left(\mathrm{SrO} + (1-x)\mathrm{TiO_2} + \frac{x}{2}\mathrm{Nb_2O_5}\right) \xrightarrow{\text{oxidizing}} \mathrm{Sr}_{1-y}(\mathrm{Ti}_{1-x}\mathrm{Nb}_x)_{1-y}\mathrm{Ni}_y\mathrm{O}_{3-((2+\frac{x}{2})y-\frac{x}{2})}, \quad (0 \le x, y \le 1) \quad (4)$$

Adding NiO introduces not only A-site deficiency, but also p-type doping (Ni'_{Ti}) to the material. Five percent of Ni (y = 0.05) can fully compensate the donor charge from STN in oxidizing atmospheres without forming Sr-rich secondary phases. This assumption is confirmed by the XRD patterns of powder samples synthesized at 1200 °C in air (Figure 1). Ni-STN exhibits single perovskite phase, while STN shows evident impurity peaks, which can be attributed to Sr-rich phases ($Sr_5Nb_4O_{15}$ (JCPDS 48-0421)), consistent with other reports.[32,35] Porous Ni-STN samples were reduced at 900 °C to demonstrate the precipitation of nanocatalyst particles. Figure 2a shows the sample reduced for 10 h, and a few nanoparticles can be seen emerged on the cross section at the grain boundaries and near grain surface. As the reduction was prolonged to 20 h, more particles can be observed, even on the grain surface, as shown in Figure 2b. Figure 2c,d shows the SEM images in higher magnifications for the sample reduced for 20 h. The preference for the nanocatalyst particles to precipitate at the grain boundaries is still evident, especially for the area far from the grain surface. However, the amount of particles generated near the surface is evidently larger. Such distribution indicates that the catalyst precipitation is significantly dependent on the degree of reduction. The typical catalyst particle near the grain surface is shown in Figure 2e, and a diameter of about 50 nm can be measured.

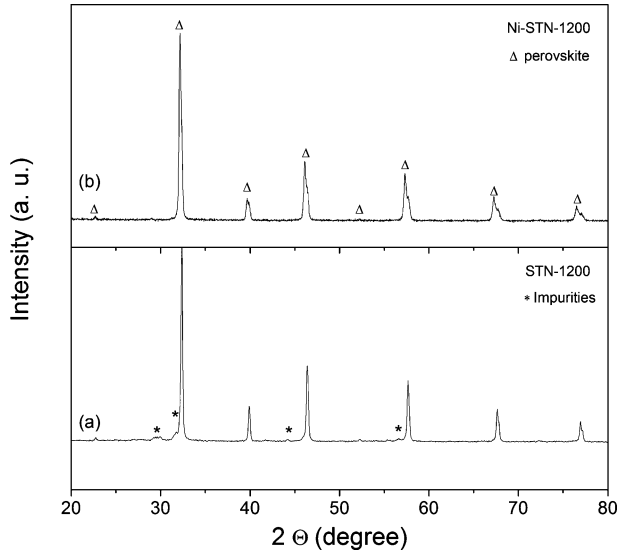

Figure 1. XRD of (a) STN and (b) Ni-STN synthesized by a solid state reaction route at 1200 °C in air.

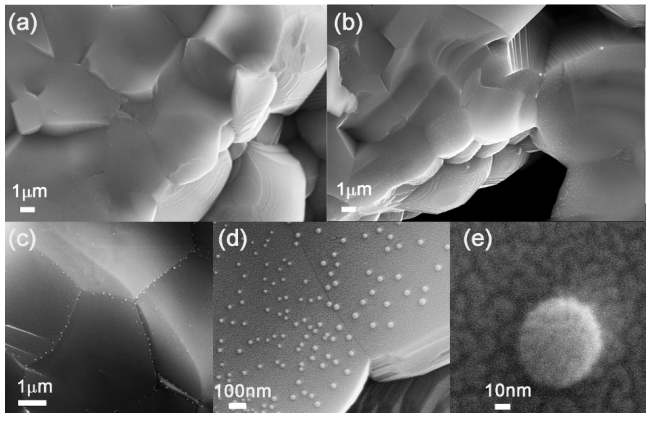

Figure 2. SEM images of Ni-STN after reduction at 900 °C in H_2 (3 vol % H_2O) for (a) 10 h and (b–e) 20 h.

Ni-STN was further reduced at 1400 °C for 10 h to accelerate the phase change. The reduced samples were studied by SEM, XPS, and Neutron powder diffraction to verify the proposed changes for Ni-STN. Figure 3a shows the SEM and EDX results of the reduced sample. Ni particles with diameters of about hundreds of nanometers can be observed due to the high treatment temperature, in contrast to the much smaller ones obtained at lower temperature. Figure 3b shows the Ni 2p core levels for Ni-STN powder samples before and after reduction at 1400 °C. Compared with those reported values, a shoulder band at 852.8 eV can be observed for the reduced sample, corresponding to the Ni metallic phase; however, most of Ni was still in the oxide form.[36] The composition of reduced ceramic phase and the metal content in reduced Ni-STN were investigated by Neutron powder diffraction to verify the proposed phase changes. Figure 3c shows the diffraction data and the Rietveld refinement result in the log–log scale. The diffraction pattern of the reduced Ni-STN can be well fitted with a cubic perovskite phase (space group $Pm\bar{3}m$) and a metallic Ni phase (space group $Fm\bar{3}m$; Rwp = 4.20%, Rp = 3.20%, χ^2 = 1.594). The fitting parameters are shown in Table 2. It can be seen that Ni has been partially extracted from the lattice after reduction at 1400 °C, resulting in 1.69(7) wt % of Ni metal in the reduced composite. According to the refinement results shown in Table 2, Ni occupancy in the reduced perovskite phase was about 0.032(2) versus 0.05 before reduction, which means a significant amount of Ni still remained in the lattice, which is consistent with the XPS analysis. The reduction of Ni-STN can be expressed by eq 5. As the transition continues, more Ni metal particles are extracted from the lattice, and the A-site deficient perovskite phase approaches more closely to the stoichiometric composition as expected.

$$\mathrm{Sr}_{0.95}(\mathrm{Ti}_{0.8}\mathrm{Nb}_{0.2})_{0.95}\mathrm{Ni}_{0.05}\mathrm{O}_{3-\delta} \xrightarrow{\text{anode}} \mathrm{Sr}_{0.95}(\mathrm{Ti}_{0.8}\mathrm{Nb}_{0.2})_{0.95}\mathrm{Ni}_{0.05-x}\mathrm{O}_{3-\delta} + x\mathrm{Ni}, \quad (0 \le x \le 0.05) \quad (5)$$

STN and Ni-STN were mixed with SDC as composite anodes, and their single-cell performance was tested in LSGM electrolyte (~300 μm) supported single cells with LDC interlayers and LSCF cathodes. The cells were activated under a constant current load of 300 mA cm^{-2} for about 80 h in H_2 to reduce the anodes before the I–V and I–P curves were recorded. As shown in Figure 4, the peak power density of STN–SDC cell at 800 °C after activation reached 341 mW cm^{-2}. Due to the modification of Ni catalysts, the cells with the Ni-STN anode exhibited almost double the peak cell power output of those with STN. Peak power densities of 612, 794, and 922 mW cm^{-2} were achieved in H_2 at 800, 850, and 900 °C, respectively. The values are much higher than those reported for strontium titanate anodes and comparable to those

dx.doi.org/10.1021/am5055417 | ACS Appl. Mater. Interfaces 2014, 6, 19990–19996

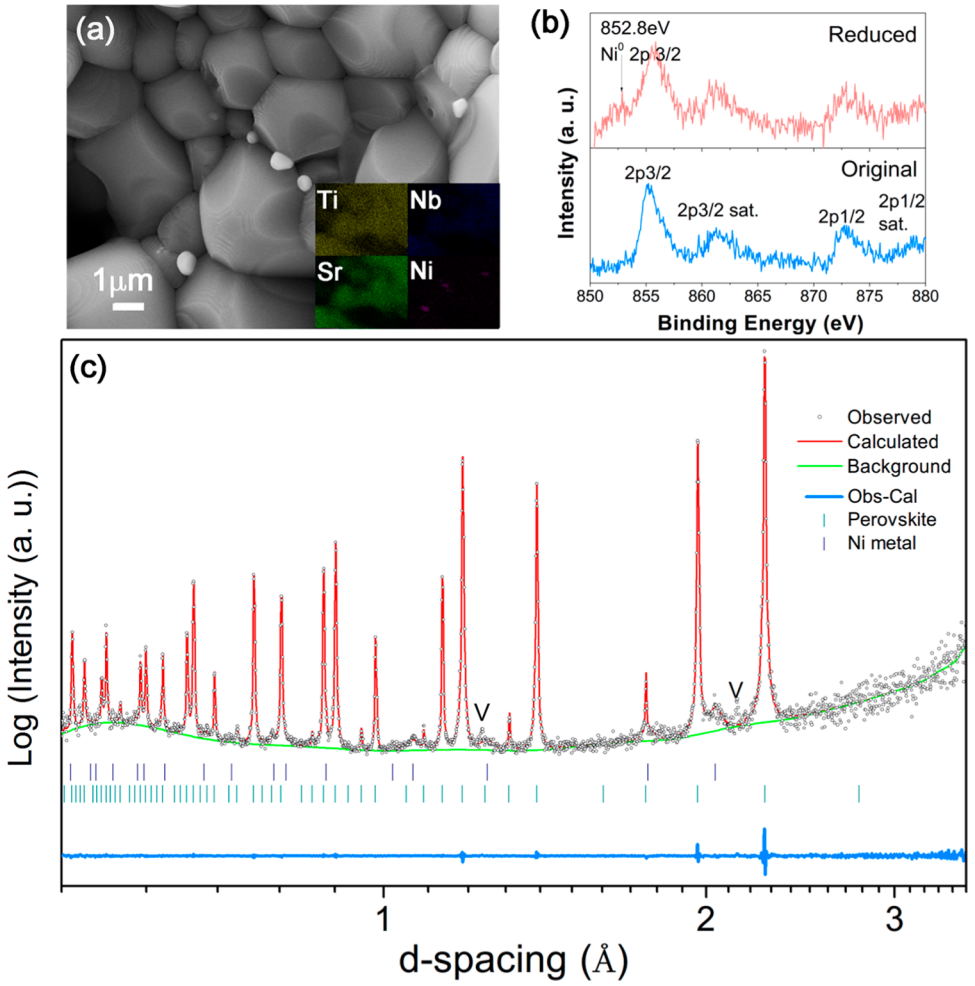

Figure 3. (a) SEM image of Ni-STN reduced at 1400 °C in 5%H_2/N_2. (b) Ni 2p core levels of Ni-STN and Ni-STN reduced at 1400 °C in 5%H_2/N_2. (c) Rietveld refinement of neutron powder diffraction for Ni-STN reduced at 1400 °C. "V" marks two visible peaks from the vanadium sample canister.

Table 2. Parameters for Rietveld Refinement of the Neutron Powder Diffraction

parameters	Sr(Ti,Nb,Ni)$O_{3-\delta}$	Ni
a (Å)	3.92918(2)	3.532(2)
occup. Sr	0.95	
occup. Ti	0.790(2)	
occup. Nb	0.155(2)	
occup. Ni	0.032(2)	
occup. O	0.971(8)	
Rwp	4.20%	
Rp	3.20%	
χ^2	1.594	
Ni wt. frac.	0.0169(7)	

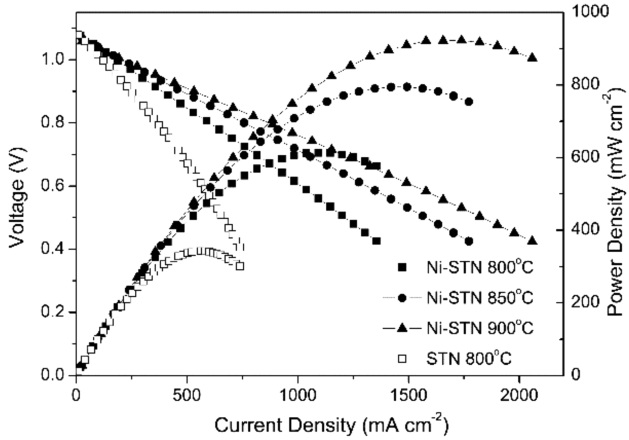

Figure 4. Cell voltages and power densities on current density of LSGM electrolyte-supported single cells for Ni-STN and STN anode in H_2.

infiltrated with small amounts of catalysts, such as 275 mW cm^{-2} at 800 °C for 1 mg cm^{-2} Ni-infiltrated $La_{0.2}Sr_{0.8}TiO_3$–$Ce_{0.9}Gd_{0.1}O_2$ anode on 300 μm thick LSGM electrolyte,[37] 577 mW cm^{-2} at 800 °C for 1.5 wt % Pd-infiltrated $Sr_{0.88}Y_{0.08}TiO_3$–LDC anode on 300 μm thick LSGM electrolyte,[38] and 640 mW cm^{-2} for 1 wt % Pd and 3 wt % CeO_2-infiltrated STN–yttria-stabilized zirconia (YSZ) anode on 50 μm thick YSZ electrolyte,[35] indicating such design strategy for Ni-STN is very effective to enhance anode performance of ceramic materials.

Due to the high dispersion of catalyst particles and the restraint of the ceramic phase in this self-generated composite, Ni-STN anode exhibited good stability under constant current load in H_2 and redox cycles. The cell was tested at 800 °C for almost 160 h in H_2 with nine redox cycles, and the results are

dx.doi.org/10.1021/am5055417 | ACS Appl. Mater. Interfaces 2014, 6, 19990–19996

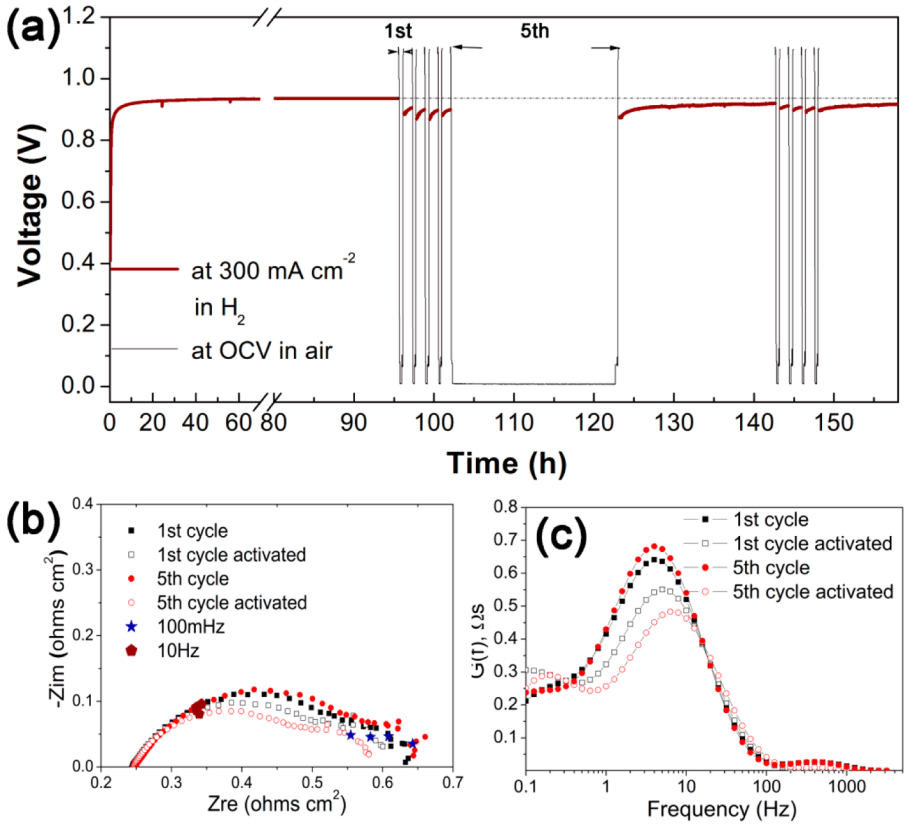

Figure 5. (a) Voltage of the cell with Ni-STN tested at 800 °C in H_2 and in redox cycling. The air exposure time was 10 min or 20 h (for the fifth cycle) during cycling. (b) Nyquist plots and (c) distributions of relaxation times of impedance spectra measured on cells with Ni-STN after the first and fifth redox cycles.

shown in Figure 5. An activation process can be observed in Figure 5a in which the cell voltage under a current load of 300 mA cm^{-2} increased dramatically in a few hours. As previously mentioned, the activation could be attributed to the reduction of Ni-STN companied with the extraction of Ni. The Ni-STN cell reached stable performance in about 30 h. The redox stability of the Ni-STN cell was investigated by switching the anode gas between H_2 and air for nine cycles with different lengths of exposure time in air after the cell was operated under a current load of 300 mA cm^{-2} in H_2 for 95 h. The oxidation impact on the cell performance is evident. A voltage drop of about 6% can be observed after a 10 min exposure in air. However, such a drop in the voltage can be recovered gradually upon operating the cell in H_2, and the voltage increased to 97% of the initial value after 1 h. The cell performance became quite stable after the first cycle, and the cell voltage recovered to above 96% of the initial value in all of the following cycles. It is interesting that prolonging the oxidation time to about 20 h in air does not further degrade the cell performance, but extending operation time in H_2 is very effective in recovering the performance. As shown in Figure 5a, the cell voltage recovered continuously to 98% of the initial value by operating the cell in H_2 for about 20 h in the fifth cycle and 10 h in the ninth cycle, indicating that the reversibility and stability of Ni-STN in redox cycling is quite impressive.

Figure 5b shows the Nyquist plots for the Ni-STN cell after the first and fifth redox cycles. Tthe major impact of redox cycling was on the polarization resistance of the cell rather than the ohmic resistance, indicating physical chemistry changes of the anode surface during redox cycling governs the degradation of the cell performance. It seems that the short exposure time in air does not change the electrode conductivity. Such resistance to oxidation was reported for several $SrTiO_3$-based materials and has been proposed as good features for redox stable materials.[39,40] As shown for the fifth redox cycle, longer oxidation time did have some negative influence on the ohmic resistance, but it is still recoverable in H_2 after adequate time. Figure 5c shows the distributions of relaxation times calculated from the impedance results to analyze the electrode processes. At least two processes occurred, corresponding to one small peak at about 400 Hz and one broad peak at 3−8 Hz. Both peaks changed upon redox cycling for the anode but the low frequency one was dominant. According to the findings by Leonide et al.,[41] this peak can be probably ascribed to the impedance contribution from the chemical process, which may be significantly affected by the catalytic activity of the anode. The intensity of the peak increased significantly after oxidation, but it can be brought down by sufficient reduction. By operating the cell in H_2 for about 20 h after the fifth cycle, the impedance is even smaller than that measured after the first cycle, showing the good reversibility of Ni-STN anode during redox cycling.

4. CONCLUSION

In conclusion, $Sr_{0.95}Ti_{0.76}Nb_{0.19}Ni_{0.05}O_{3-\delta}$ (Ni-STN) was formed by combining NiO with stoichiometric $SrTi_{0.8}Nb_{0.2}O_{3-\delta}$. Upon reduction, Ni-STN released Ni particles, and the ceramic composition approached $SrTi_{0.8}Nb_{0.2}O_{3-\delta}$ without forming undesired secondary phases. The simple material design strategy gives good control of the ceramic phase in the self-

generated metal-ceramic composites. Benefiting from the catalytic active nano metallic phase and the stability of the ceramic backbone, enhanced fuel cell performance and excellent redox stability were achieved.

AUTHOR INFORMATION

Corresponding Author

*Tel: +1-803-777-4875. Fax: +1-803-777-0106. E-mail: chenfa@cec.sc.edu.

Notes

The authors declare no competing financial interest.

ACKNOWLEDGMENTS

We are grateful to the financial support from the U.S. National Science Foundation (DMR-1210792). The Research at Oak Ridge National Laboratory's Spallation Neutron Source was sponsored by the Scientific User Facilities Division, Office of Basic Energy Sciences, U.S. Department of Energy.

REFERENCES

(1) Wachsman, E. D.; Marlowe, C. A.; Lee, K. T. Role of Solid Oxide Fuel Cells in a Balanced Energy Strategy. *Energy Environ. Sci.* **2012**, *5*, 5498−5509.

(2) Gorte, R. J.; Park, S.; Vohs, J. M.; Wang, C. H. Anodes for Direct Oxidation of Dry Hydrocarbons in a Solid-Oxide Fuel Cell. *Adv. Mater.* **2000**, *12*, 1465−1469.

(3) Sarantaridis, D.; Atkinson, A. Redox Cycling of Ni-Based Solid Oxide Fuel Cell Anodes: A Review. *Fuel Cells* **2007**, *7*, 246−258.

(4) Blinn, K. S.; Abernathy, H.; Li, X. X.; Liu, M. F.; Bottomley, L. A.; Liu, M. L. Raman Spectroscopic Monitoring of Carbon Deposition on Hydrocarbon-Fed Solid Oxide Fuel Cell Anodes. *Energy Environ. Sci.* **2012**, *5*, 7913−7917.

(5) Yokokawa, H.; Yamaji, K.; Brito, M. E.; Kishimoto, H.; Horita, T. General Considerations on Degradation of Solid Oxide Fuel Cell Anodes and Cathodes Due to Impurities in Gases. *J. Power Sources* **2011**, *196*, 7070−7075.

(6) Ettler, M.; Timmermann, H.; Malzbender, J.; Weber, A.; Menzler, N. H. Durability of Ni Anodes during Reoxidation Cycles. *J. Power Sources* **2010**, *195*, 5452−5467.

(7) Faes, A.; Hessler-Wyser, A.; Zryd, A. A Review of Redox Cycling of Solid Oxide Fuel Cells Anode. *Membranes* **2012**, *2*, 585−664.

(8) Tao, S. W.; Irvine, J. T. S. A Redox-Stable Efficient Anode for Solid-Oxide Fuel Cells. *Nat. Mater.* **2003**, *2*, 320−323.

(9) Fu, Q. X.; Tietz, F. Ceramic-based Anode Materials for Improved Redox Cycling of Solid Oxide Fuel Cells. *Fuel Cells* **2008**, *8*, 283−293.

(10) Liu, Q. A.; Dong, X. H.; Xiao, G. L.; Zhao, F.; Chen, F. L. A Novel Electrode Material for Symmetrical SOFCs. *Adv. Mater.* **2010**, *22*, 5478−5482.

(11) Liu, Q.; Bugaris, D. E.; Xiao, G. L.; Chmara, M.; Ma, S. G.; zur Loye, H. C.; Amiridis, M. D.; Chen, F. L. $Sr_2Fe_{1.5}Mo_{0.5}O_{6-\delta}$ as a Regenerative Anode for Solid Oxide Fuel Cells. *J. Power Sources* **2011**, *196*, 9148−9153.

(12) Xiao, G.; Chen, F. Ni Modified Ceramic Anodes for Direct-Methane Solid Oxide Fuel Cells. *Electrochem. Commun.* **2011**, *13*, 57−59.

(13) Xiao, G.; Jin, C.; Liu, Q.; Heyden, A.; Chen, F. Ni Modified Ceramic Anodes for Solid Oxide Fuel Cells. *J. Power Sources* **2012**, *201*, 43−48.

(14) Bi, Z. H.; Zhu, J. H. Effect of Current Collecting Materials on the Performance of the Double-Perovskite $Sr_2MgMoO_{6-\delta}$ Anode. *J. Electrochem. Soc.* **2011**, *158*, B605−B613.

(15) Zhu, X.; Lu, Z.; Wei, B.; Chen, K. F.; Liu, M. L.; Huang, X. Q.; Su, W. H. Enhanced Performance of Solid Oxide Fuel Cells with Ni/CeO_2 Modified $La_{0.75}Sr_{0.25}Cr_{0.5}Mn_{0.5}O_{3-\delta}$ Anodes. *J. Power Sources* **2009**, *190*, 326−330.

(16) Smith, B. H.; Gross, M. D. A Highly Conductive Oxide Anode for Solid Oxide Fuel Cells. *Electrochem. Solid-State Lett.* **2011**, *14*, B1−B5.

(17) Lee, S.; Miller, N.; Gerdes, K. Long-Term Stability of SOFC Composite Cathode Activated by Electrocatalyst Infiltration. *J. Electrochem. Soc.* **2012**, *159*, F301−F308.

(18) Madsen, B. D.; Kobsiriphat, W.; Wang, Y.; Marks, L. D.; Barnett, S. A. Nucleation of Nanometer-Scale Electrocatalyst Particles in Solid Oxide Fuel Cell Anodes. *J. Power Sources* **2007**, *166*, 64−67.

(19) Kobsiriphat, W.; Madsen, B. D.; Wang, Y.; Shah, M.; Marks, L. D.; Barnett, S. A. Nickel- and Ruthenium-Doped Lanthanum Chromite Anodes: Effects of Nanoscale Metal Precipitation on Solid Oxide Fuel Cell Performance. *J. Electrochem. Soc.* **2010**, *157*, B279−B284.

(20) Boulfrad, S.; Cassidy, M.; Irvine, J. T. S. $NbTi_{0.5}Ni_{0.5}O_4$ as Anode Compound Material for SOFCs. *Solid State Ionics* **2011**, *197*, 37−41.

(21) Bierschenk, D. M.; Potter-Nelson, E.; Hoel, C.; Liao, Y. G.; Marks, L.; Poeppelmeier, K. R.; Barnett, S. A. Pd-substituted $(La,Sr)CrO_{3-\delta}$-$Ce_{0.9}Gd_{0.1}O_{2-\delta}$ Solid Oxide Fuel Cell Anodes Exhibiting Regenerative Behavior. *J. Power Sources* **2011**, *196*, 3089−3094.

(22) Neagu, D.; Tsekouras, G.; Miller, D. N.; Menard, H.; Irvine, J. T. S. In Situ Growth of Nanoparticles through Control of Non-Stoichiometry. *Nat. Chem.* **2013**, *5*, 916−923.

(23) Xiao, G.; Wang, S.; Lin, Y.; Yang, Z.; Han, M.; Chen, F. Ni-doped $Sr_2Fe_{1.5}Mo_{0.5}O_{6-\delta}$ as Anode Materials for Solid Oxide Fuel Cells. *J. Electrochem. Soc.* **2014**, *161*, F305−F310.

(24) Xiao, G.; Chen, F. Redox Stable Anodes for Solid Oxide Fuel Cells. *Front. Energy Res.* **2014**, *2*, 18.1−18.13.

(25) Huang, T. J.; Chou, C. L.; Chen, W. J.; Huang, M. C. Coal Syngas Reactivity over Ni-added LSCF−GDC Anode of Solid Oxide Fuel Cells. *Electrochem. Commun.* **2009**, *11*, 294−297.

(26) An, K.; Skorpenske, H.; Stoica, A.; Ma, D.; Wang, X. L.; Cakmak, E. First in-situ lattice strains measurements under load at VULCAN. *Metall. Mater. Trans. A* **2011**, *42* (1), 95−99.

(27) An, K. VDRIVE- Data Reduction and Interactive Visualization Software for Event Mode Neutron Diffraction, *ORNL Report*, Oak Ridge National Laboratory; 2012, *Vol. ORNL-TM-2012-621*.

(28) Toby, B. H. EXPGUI, A Graphical User Interface for GSAS. *J. Appl. Crystallogr.* **2001**, *34*, 210−213.

(29) Kolodiazhnyi, T.; Petric, A. The Applicability of Sr-deficient n-Type $SrTiO_3$ for SOFC Anodes. *J. Electroceram.* **2005**, *15*, 5−11.

(30) Hui, S.; Petric, A. Evaluation of Yttrium-Doped $SrTiO_3$ as an Anode for Solid Oxide Fuel Cells. *J. Eur. Ceram. Soc.* **2002**, *22*, 1673−1681.

(31) Marina, O. A.; Canfield, N. L.; Stevenson, J. W. Thermal, Electrical, and Electrocatalytical Properties of Lanthanum-Doped Strontium Titanate. *Solid State Ionics* **2002**, *149*, 21−28.

(32) Xiao, G.; Nuansaeng, S.; Zhang, L.; Suthirakun, S.; Heyden, A.; Loye, H.-C. z.; Chen, F. Enhanced Reducibility and Conductivity of Na/K-Doped $SrTi_{0.8}Nb_{0.2}O_3$. *J. Mater. Chem. A* **2013**, *1*, 10546−10552.

(33) Suthirakun, S.; Ammal, S. C.; Xiao, G.; Chen, F.; zur Loye, H. C.; Heyden, A. Density Functional Theory Study on the Electronic Structure of n- and p-Type Doped $SrTiO_3$ at Anodic Solid Oxide Fuel Cell Conditions. *Phys. Rev. B* **2011**, *84*, 205102.1−205102.9.

(34) Yang, C.; Yang, Z.; Jin, C.; Xiao, G.; Chen, F.; Han, M. Sulfur-Tolerant Redox-Reversible Anode Material for Direct Hydrocarbon Solid Oxide Fuel Cells. *Adv. Mater.* **2012**, *24*, 1439−1443.

(35) Gross, M. D.; Carver, K. M.; Deighan, M. A.; Schenkel, A.; Smith, B. M.; Yee, A. Z. Redox Stability of $SrNb_xTi_{1-x}O_3$−YSZ for Use in SOFC Anodes. *J. Electrochem. Soc.* **2009**, *156*, B540−B545.

(36) Grosvenor, A. P.; Biesinger, M. C.; Smart, R. S.; McIntyre, N. S. New Interpretations of XPS Spectra of Nickel Metal and Oxides. *Surf. Sci.* **2006**, *600*, 1771−1779.

(37) Yoo, K. B.; Choi, G. M. Performance of La-Doped Strontium Titanate (LST) Anode on $LaGaO_3$-based SOFC. *Solid State Ionics* **2009**, *180*, 867−871.

(38) Lu, X. C.; Zhu, J. H.; Yang, Z.; Xia, G.; Stevenson, J. W. Pd-Impregnated SYT/LDC Composite as Sulfur-Tolerant Anode for Solid Oxide Fuel Cells. *J. Power Sources* **2009**, *192*, 381−384.
(39) Hashimoto, S.; Poulsen, F. W.; Mogensen, M. Conductivity of SMO_3-Based Oxides in the Reducing Atmosphere at High Temperature. *J. Alloys Compd.* **2007**, *439*, 232−236.
(40) Li, X.; Zhao, H.; Shen, W.; Gao, F.; Huang, X.; Li, Y.; Zhu, Z. Synthesis and Properties of Y-Doped $SrTiO_3$ as an Anode Material for SOFCs. *J. Power Sources* **2007**, *166*, 47−52.
(41) Leonide, A.; S, V.; Weber, A.; Ivers-Tiffée, E. Evaluation and Modeling of the Cell Resistance in Anode-Supported Solid Oxide Fuel Cells. *J. Electrochem. Soc.* **2008**, *155*, B36−B41.